

A New Insight into Growth Mechanism and Kinetics of Mesoporous Silica Nanoparticles by in Situ Small Angle X-ray Scattering

Zhifeng Yi,[†] Ludovic F. Dumée,[†] Christopher J. Garvey,^{*,‡} Chunfang Feng,[†] Fenghua She,[†] James E. Rookes,[§] Stephen Mudie,^{||} David M. Cahill,[§] and Lingxue Kong^{*,†}

[†]Institute for Frontier Materials, Deakin University, Geelong Campus at Waurn Ponds, Geelong, Victoria 3216, Australia

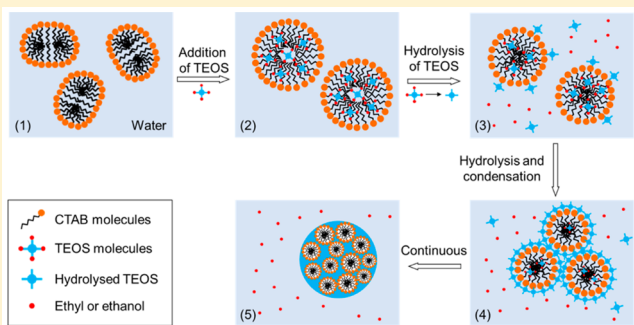
[‡]Australian Nuclear Science and Technology Organization, Lucas Heights, New South Wales 2234, Australia

[§]Centre for Chemistry and Biotechnology, School of Life and Environmental Sciences, Deakin University, Geelong Campus at Waurn Ponds, Geelong, Victoria 3216, Australia

^{||}Australian Synchrotron, 800 Blackburn Road, Clayton, Victoria 3169, Australia

S Supporting Information

ABSTRACT: The growth mechanism and kinetics of mesoporous silica nanoparticles (MSNs) were investigated for the first time by using a synchrotron time-resolved small-angle X-ray scattering (SAXS) analysis. The synchrotron SAXS offers unsurpassed time resolution and the ability to detect structural changes of nanometer sized objects, which are beneficial for the understanding of the growth mechanism of small MSNs (~20 nm). The Porod invariant was used to quantify the conversion of tetraethyl orthosilicate (TEOS) in silica during MSN formation, and the growth kinetics were investigated at different solution pH and temperature through calculating the scattering invariant as a function of reaction time. The growth of MSNs was found to be accelerated at high temperature and high pH, resulting in a higher rate of silica formation. Modeling SAXS data of micelles, where a well-defined electrostatic interaction is assumed, determines the size and shape of hexadecyltrimethylammonium bromide (CTAB) micelles before and after the addition of TEOS. The results suggested that the micelle size increases and the micelle shape changes from ellipsoid to spherical, which might be attributed to the solubilization of TEOS in the hydrophobic core of CTAB micelles. A new “swelling–shrinking” mechanism is proposed. The mechanism provides new insights into understanding MSN growth for the formation of functional mesoporous materials exhibiting controlled morphologies. The SAXS analyses were correlated to the structure of CTAB micelles and chemical reaction of TEOS. This study has provided critical information to an understanding of the growth kinetics and mechanism of MSNs.



1. INTRODUCTION

The high porosity and accessible surface functionalization of mesoporous silica nanoparticles (MSNs) have opened a new route to the formation of porous supports for the decoration with high performance catalysts¹ and a potential platform for advanced biomolecule carriers for targeted and controlled drug delivery systems.^{2,3} A variety of sol–gel processes have been developed to synthesize ordered meso-structured silica frameworks with highly tuneable properties and morphologies from surfactant templates including parallel hexagonal mesochannels, radially oriented mesopores and hierarchical mesostructures.^{4,5} The MSNs with particle size less than 30 nm in diameter^{6–8} have higher permeability across biological cell membranes, better biocompatibility and faster degradation than larger particles.^{9–11} The appropriate understanding of the growth mechanism will provide useful knowledge to design and tailor particles of smaller size and unique porous morphology for a broad range of applications.

Current theory of pathways for MSN growth have been developed for large MSNs of over 100 nm in diameter and with ordered porous structure exhibiting hexagonal or cubic mesopores.^{12–17} Previous studies suggest that the growth of the mesostructure starts from small cylindrical particles (around 6.2 nm) which assemble to form the final hexagonal structure,¹⁷ or there is a micelle shape transition from sphere to rod prior to the final formation of the mesostructure.¹² However, MSNs with a particle size at around 20 nm in diameter do not possess long-range ordered mesopores,¹⁸ and the models used to predict the growth of hexagonal structures cannot be used to describe the formation mechanism of particles at below the 20 nm scale.

The major challenge in the investigation of small MSN growth lies in the determination of kinetic parameters and the

Received: May 5, 2015

Revised: July 8, 2015

Published: July 9, 2015

growth mechanism, which requires both high spatial resolution and fast data acquisition. Conventional techniques to study the formation mechanisms of MSNs include high resolution transmission electron microscopy,¹⁹ and nuclear magnetic resonance (NMR),¹⁴ which are limited for kinetics measurements and typically require complex procedures to prepare samples. Dynamic light scattering (DLS)²⁰ has been used to determine the growth kinetics and mechanism of silica nanoparticles, but the signal from the surfactant template has a high impact on the detection of silica growth. Furthermore, the aggregation of particles with average size below the 100 nm benchmark was shown to be detrimental to both sample preparation and the determination of growth kinetics.²⁰ Due to artifacts arising from the cluster formation, there are considerable challenges to interpret the growth mechanism by these classical characterization techniques.²⁰ It is therefore critical to develop new characterization routes that allow for high resolution and real time investigation of MSN growth.

Small angle scattering techniques have been shown to be appropriate characterization tools for the morphological resolution of nanostructures and combine nondestructive statistical detection of structural changes with potential time-resolved ability.²¹ The fast data acquisition offered by synchrotron sources can achieve a subsecond resolution and provide information about the reaction kinetics or mechanism related to structural changes.^{22,23} The mechanism of MSN growth has recently been studied through time-resolved small angle neutron scattering (SANS).^{18,24} Even though the unique contrast variation provided by SANS can separate the scattering contributions from silica and surfactant phase, deuterated surfactants did not provide an adequate proxy for the normal synthesis of MSNs.¹⁸ Due to much higher fluxes, synchrotron small-angle X-ray scattering (SAXS) offers similar capabilities to SANS to make *in situ* measurement but with greater sensitivity and can therefore reveal the growth of MSNs under real conditions without any special treatment of reaction ingredients.²¹ Therefore, time-resolved synchrotron SAXS offers the benefit of precise detection of the MSNs during growth.

MSNs are normally formed by hydrolysis and condensation of the silica source on the surface of micelles formed by surfactant self-assembly in aqueous solution.^{12,13,15} A current bun model¹⁸ has been developed to describe the formation mechanism. It is proposed the hydrolyzed silica source either assembles electrostatically on to cationic micelles,¹⁹ or initially forms silica polymer but then binds onto nonionic micelles.²⁵ The condensation of silica then induces the aggregation of micelles to form larger particles. The commonly used silica precursor in aqueous MSN synthesis, the oil-like tetraethyl orthosilicate (TEOS) may cause phase separation with the aqueous solution.²⁶ Existing mechanism studies have not examined if TEOS hydrolyses by forming oil droplets in the aqueous solution or by inserting into the hydrophobic cores of micelles.^{18,27} The interactions between the micelles and the silica precursor upon hydrolysis and condensation is critical to accurately understand and predict the final morphology of MSNs.

Herein, the growth kinetics and mechanism of these small MSNs are dynamically investigated through time-resolved synchrotron SAXS. The effects of experimental conditions including pH, temperature and ionic strength on the growth kinetics of MSNs were investigated. The scattering invariant and a simple two-phase approximation were utilized as a simple but powerful tool to interpret the growth kinetics of the

particles under the corresponding experimental conditions. In addition, through modeling the SAXS data of micelles before and after TEOS addition, a swelling–shrinking mechanism of MSNs was proposed, which could provide systematic information of the formation of MSNs and greatly benefit the future work on controlling the characteristics of MSNs and the design of novel meso-structures.

2. MATERIALS AND METHODOLOGY

2.1. Materials. Cetyltrimethylammonium bromide (CTAB, ≥99%) and tetraethyl orthosilicate (TEOS, 98%) were purchased from Sigma-Aldrich. Sodium hydroxide (NaOH), potassium dihydrogen phosphate (KH_2PO_4), ammonia hydroxide, ethanol and hydrochloric acid were AR grade. All the chemicals were used without further purification. Quartz capillary tubes (20 mm in length, outside diameter of 2.5 mm and wall thickness of 0.01 mm) were purchased from Charles Supper Company (Natick).

2.2. Synthesis Procedures of MSNs. All the experimental parameters are listed in Table 1. The MSNs were synthesized in

Table 1. Experimental Parameters for Each Setup of *in Situ* Experiments

samples	CTAB (mM)	TEOS (mM)	T (°C)	pH	time (min)
30-7.2	80	80	30	7.2 ^a	150
95-7.2	80	80	95	7.2 ^a	57
30-10-H ^b	80	80	30	10	150
30-10-L ^c	80	80	30	10	150

^aThe pH value of the buffer solution was 7.2. ^bThe pH value of the buffer solution was adjusted to 10 by adding sodium hydroxide. Because of the increased salt concentration, the ionic strength of this sample is the highest (0.16 mol/L·electron²), which is denoted as H.

^cThe pH value of this experimental set was adjusted to 10 with ammonium hydroxide. Without any salt in this solution, the ionic strength of this sample is the lowest (0.00005 mol/L·electron²), which is denoted as L.

aqueous solution by using self-assembled CTAB as templates to generate silica mesoporous structure.^{28–30} The effects of temperature on the growth of MSNs were investigated at 30 and 95 °C. Those temperatures are respectively the lowest temperature at which CTAB can form micelles avoiding the slow crystallization at 25 °C (Krafft temperature³¹) and the extreme temperature that can be achieved before boiling. Other conditions, such as pH and ionic strength, can affect the hydrolysis and condensation rate of TEOS, leading to a different MSN growth rate. The pH was controlled by changing the base concentration in the phosphate buffer solution. Weak bases were utilized as catalysts,^{11,32} in order to examine MSN growth under extremely low ionic strength. The specific synthesis procedures were described as follows.

2.2.1. Synthesis of MSNs under Neutral Condition (pH = 7.2). The buffer solution was obtained from mixing 1.74 g of NaOH and 10.2 g of KH_2PO_4 in 1.5 L of Milli-Q water (final pH value is 7.2). CTAB (2.96 g) was dissolved in 100 mL of this buffer solution. The mixture was heated to and remained at 80 °C for 30 min to stabilize CTAB micelles. Subsequently, the aqueous solution of CTAB was cooled to 30 °C followed by dropwise addition of 1.86 mL of TEOS. The reaction was maintained for a certain period under stirring. To examine the growth kinetics of MSNs at high temperature, one batch of MSNs was synthesized at 95 °C and the particle size was increased to ~50 nm under this condition. For this purpose the stabilized CTAB solution was heated to 95 °C before adding TEOS and the same procedures as for the synthesis of MSNs under pH 7.2 was followed.

2.2.2. Synthesis of MSNs under Basic Condition (pH = 10). The CTAB (2.96 g) was dissolved in 100 mL of the above buffer solution. The pH was adjusted to 10 using sodium hydroxide. The mixture was heated to and remained at 80 °C and then kept stirring for 30 min in

order to stabilize the structure of CTAB micelles. Subsequently, the aqueous CTAB solution was cooled to 30 °C followed by dropwise addition of 1.86 mL of TEOS. The reaction was maintained for 150 min while stirring. For the synthesis of MSNs in ammonia, the buffer solution was replaced with a solution of ammonia (pH = 10). The rest of the procedures was the same as the synthesis of MSNs in the buffer solution.

2.3. Setup of Time-Resolved Synchrotron SAXS. SAXS experiments were conducted on the SAXS beamline at the Australian Synchrotron. A Pilatus 1 M detector was used for all SAXS data collection. The sample-detector distance was 1.6 m, and the energy was adjusted to 9 keV to cover a Q range of 0.008–0.45 Å⁻¹. Q is the scattering vector which is defined as $Q = 4\pi(\sin \theta)/\lambda$, where 2θ is the angle between the incident beam and the scattering on the detector and λ is the wavelength of the X-ray. The distance from the sample to detector was calibrated with a silver behenate standard. After masking the regions of the detector covered by the beam stop, hot pixels and gaps between detector modules the isotropic counts on the Pilatus detector were radially averaged around the direction of the primary beam and converted to the intensity versus Q by using the measurement geometry of beam line software (Scatterbrain). An appropriate background collected from the capillary tubes filled with reaction solution (phosphate buffer or ammonium hydroxide) was subtracted from each scattering curve. The scattering intensity was calibrated in units of absolute intensity using Milli-Q water as the standard.

The dynamic investigation of MSN growth was made using a specially designed setup which allowed remote initiation of the chemical reaction directly on the SAXS beamline and avoided damage to samples as observed when using a continuous flow system.^{14,16,22} The schematic of the setup is shown in Figure 1. Specifically, MSNs

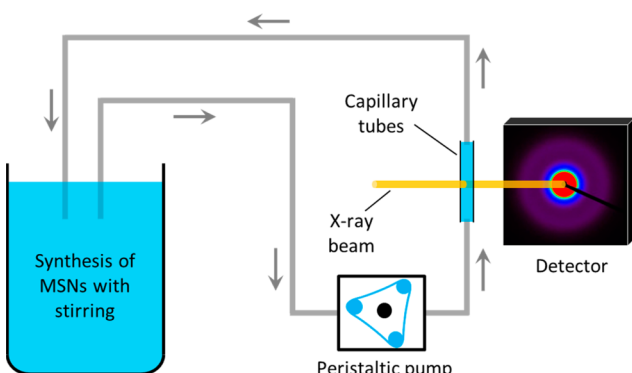


Figure 1. SAXS setup to dynamically monitor the growth of MSNs under different experimental conditions. The temperature of the reservoir for fabricating MSNs was controlled by a water bath with magnetic stirrer. The circulated reaction liquid came from the bottom of capillary tubes to the top in order to eliminate any influence of bubbles generated by the influent fluidic flow.

were synthesized in a 200 mL beaker in a water bath to control the temperature of the reaction mixture. During the fabrication of MSNs, the mixture solution was circulated through a peristaltic pump with a flow rate of 0.5 mL/s between the reaction reservoir and capillary tubes. The length of pipes was 2.8 m and the diameter was 2.5 mm. By considering the pipe length, diameter and flow rate, the mixing dead time was estimated to be shorter than 30 s. SAXS patterns were collected from the quartz capillary tubes for 2 s every 28 s for 150 min (300 patterns) in order to match the circulation time and to obtain best resolution at 30 °C. Since a steady state in the SAXS patterns was reached faster at 95 °C, the total data acquisition was for ~1 h.

2.4. Modeling of CTAB Micelles. The SAXS data of CTAB micelles in different solutions were modeled in the software of "SASview" (version 3.0.0) via a least-squares fitting and appropriate constraint of the model. The total intensity ($I(Q)$) was interpreted by the following equation:

$$I(Q) = P(Q) \otimes S(Q) + \text{background} \quad (1)$$

where, $P(Q)$ is the form factor related to the shape of the micelles in the solution and $S(Q)$ is the structure factor associated with the interaction between micelles.³³

2.4.1. Modeling of CTAB Micelles before TEOS Addition. The CTAB micelles tend to form an ellipsoid shape in aqueous solution with the hydrophilic head groups and condensed counterions being considered as an electron dense shell around the core formed by the hydrophobic tails. Thus an ellipsoid core–shell model with fixable shell thickness was used to fit the SAXS data of CTAB micelles in the aqueous solution. This model proved to be ideal to fit the SAXS data of CTAB under different experimental conditions in this study. The ellipsoid core–shell form factor was given by^{34,35}

$$P(Q) = \frac{\text{scale}}{V} \int_0^1 |F(Q, r_{\min}, r_{\text{maj}}, \alpha)|^2 d\alpha + \text{background} \quad (2)$$

where, "scale" is the scale factor, V is the volume of the ellipse that can be calculated by $V = (4/3)\pi r_{\text{maj}} r_{\min}^2$, r_{\min} and r_{maj} are the minor and major radius of the ellipse, respectively, and α is the angle between the major axis and the Q vector.

In the absence of added salt the interaction between neighboring CTAB micelles is related to electrostatic repulsions because of the net charges on the surface of the micelles screened by the unbound counterions. This interaction leads to the presence of $S(Q)$ that was calculated from a model of rescaled mean spherical approximation (RMSA) reported by Hayter and Penfold.^{36,37} This model is based on screened electrostatic interactions between charged particles in the presence of counter-ions and the amount of salt added to the solution. They were defined by the following parameters: the volume fraction of the hard sphere, the micellar charge, the radius of particles and the Debye length.

Several physical parameters were constrained to meet the structural assumption according to the real micellar structure.³⁸ First, the core of the micelles is considered to be formed by hydrocarbon tails of CTAB without any water penetration (hydrocarbon density). Thus, the scattering length density (SLD) of the core was constrained for this oil-like phase. Also, the SLD of water was constrained with the consideration of the effects from added salt on the electron density. Other physical properties of the system can be also constrained. These parameters include the dielectric constant of water, system temperature and volume fraction of CTAB. All the model constraints are listed in Supporting Information (SI) Table S1. The other parameters including the ellipticity of CTAB micelles, shell thickness and the charge on the surface of micelles are included in the modeling.

2.4.2. Modeling of CTAB Micelles after TEOS Addition. After the addition of TEOS, a core–shell sphere model was chosen to fit the SAXS data, which is given by³⁹

$$P(Q) = \frac{\text{scale}}{V_s} (F_{\text{core}} + F_{\text{shell}})^2 + \text{background} \quad (3)$$

$$F_{\text{core}} = 3V_c(\rho_c - \rho_s) \frac{[\sin(qr_c) - qr_c \cos(qr_c)]}{(qr_c)^3} \quad (4)$$

$$F_{\text{shell}} = 3V_s(\rho_s - \rho_{\text{solv}}) \frac{[\sin(qr_s) - qr_s \cos(qr_s)]}{(qr_s)^3} \quad (5)$$

where, "scale" is the scale factor, V_c and V_s are the volume of the core and shell, r_c and r_s are the radius of the core and shell, and ρ_c , ρ_s , and ρ_{solv} are the SLD of the core, shell, and the solvent, respectively.

The TEOS is assumed to be solubilized inside the micelle core due to its hydrophobicity.⁴⁰ Accordingly, the SLD of the core should change and can be calculated from the ratio between CTAB and TEOS. At the initial stage, since the silica covered on the surface of the CTAB micelles only changes the surface charge density, Hayter–Penfold RMSA can still be used to model $S(Q)$ and to interpret the interaction between micelles. The input parameters for this model are listed in SI Table S1.

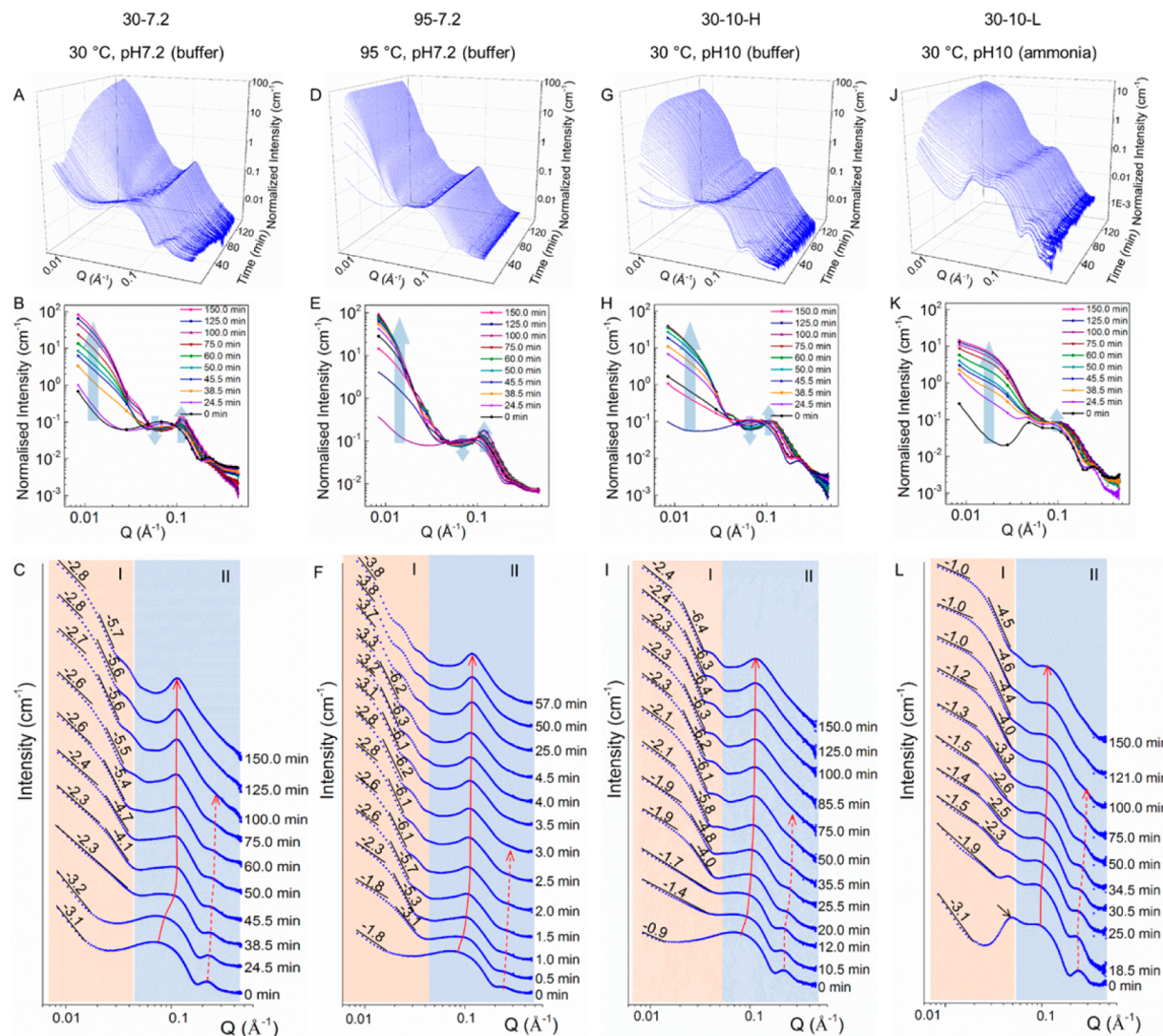


Figure 2. 3D graphs of dynamic monitoring of MSN growth with time for sample 30-7.2 (A), 95-7.2 (B), 30-10-H (C) and 30-10-L (D). Superimposed (B, E, H, and K) and shifted (C, F, I, and L) scattering curves for corresponding samples at the selected time points. These time points were selected according to the changes of the scattering curves. Similar criteria have been applied to the other samples and the figures are listed in the Supporting Information.

2.5. Calculation of Porod Invariant over Time. Porod invariants of SAXS profiles were calculated by the software SASview from selected scattering patterns at characteristic time points. The Guinier and Power law³⁹ was utilized to extrapolate the SAXS data at low and high Q , respectively to cover a total Q range between 10^{-5} and 10 \AA^{-1} .

2.6. Further Treatment and Characterization of MSN Samples. The CTAB templates inside pores were removed by soaking all the samples in a solution of 100 mL of ethanol and 1 mL of hydrochloric acid at 60 °C for 12 h. Subsequently, all samples without CTAB were centrifuged at 8000 rpm for 10 min and washed with ethanol for three times. The MSNs were dried under vacuum. The morphology of fabricated nanoparticles was characterized under a JEM 2100 transmission electron microscope (TEM) (JEOL, Japan) with an accelerating voltage of 200 kV. All samples were dispersed in absolute ethanol and dropped onto a copper grid with carbon film (Zhongjingkeyi Technology Co. Ltd, China). All the samples on copper grids were dried at room temperature until the ethanol was completely evaporated.

3. RESULTS AND DISCUSSION

3.1. Growth Kinetics of MSNs. The MSNs fabricated in this study were spherical nanoparticles that exhibited an average diameter of ~20 nm at 30 °C and ~50 nm at 95 °C, and a pore size distribution of 2 to 3 nm. Representative TEM micrographs of the MSNs, synthesized under the experimental conditions given in Table 1, are shown in SI Figure S1. Although an increase in synthesis temperature to 95 °C led to larger particle size (~50 nm), this sample has provided the information not only about the growth kinetics at high temperature, but also about the effects of temperature on the final morphology of MSNs when other conditions (TEOS and CTAB concentration, time, and pH) were kept constant.

The growth of MSNs was monitored *in situ* by time-resolved synchrotron SAXS which has a high flux but a low noise background, allowing for fast data acquisition to elaborate structural investigations. The hydrolysis and condensation rates of TEOS determine the growth kinetics of MSNs and can be examined statically in the volume of sample. Important structural changes which relate to pore size and particle size

can be noted with respect to growth time across the time-resolved graphs (**Figure 2**). The three-dimensional (3D) figures present temporal changes of scattering patterns, while the 2D figures clearly illustrate the detailed evolution of structures against each time point.

The scattering patterns can be divided into two regions based on the structure of the MSNs. The first region (region I in **Figure 2 C, F, I and L**) shows a broad shoulder between 0.01 and 0.05 Å⁻¹, which is related to the growth of the particles. The intensity of the shoulder from the particles steadily increases over time during the growth. In order to indicate the changes in curvature, the slopes of log–log plot before and after the shoulder are shown in region I in **Figure 2 C, F, I, and L**. When the curvature of the knee at 0.016 Å⁻¹ becomes constant (the slopes do not change), the outer diameter of the particles was no longer growing, implying that the formation of the particles was fully achieved. The growth of the particles was completed after 2.5 min at 95 °C as the hydrolysis and condensation rates of TEOS were highly accelerated, while the completion times for samples synthesized at 30 °C, namely, 30-7.2, 30-10-H, and 30-10-L, were 100, 75, and 100 min, respectively.

The peak representing the structure factor of CTAB micelles³⁴ (region II in **Figure 2C, F, I, and L**) progressively disappeared during MSN growth due to the condensed silica outside the micelles changing the interaction between micelles (structure factor). As seen in **Figure 2C**, when MSNs were synthesized at 30 °C and pH 7.2, the intensity of the peak corresponding to the structure factor of CTAB micelles at around 0.075 Å⁻¹ gradually decreased upon the formation of silica mesopores prior to completely disappearing after 39 min. With the temperature increased to 95 °C at pH 7.2, the intensity of the CTAB peak dramatically decreased before disappearing at 0.5 min (**Figure 2F**), highlighting the completion of the reaction. With the pH increasing up to 10 but at different ionic strength, the peak at around 0.075 Å⁻¹ disappears after 12 min for samples with higher ionic strength (30-10-H) (**Figure 2I**) and 19 min for samples with lower ionic strength (30-10-L) (**Figure 2L**). These similar pore formation rates suggest a similar reaction altitude at the same pH value. In parallel to the progressive reduction and final disappearance of the peak representing micelles, the intensity of the diffraction peak at 0.15 Å⁻¹ is attributed to the formation of silica mesopores. The presence of the diffraction peaks generated from the mesopores is visible during particle formation and can be seen on the stacked graphs (**Figure 2C, F, I, and L**). The determination of reaction stage during MSN growth is complex and requires the simultaneous knowledge of a number of parameters. Multiple models are involved, in order to interpret those structural changes in terms of pore formation, particle growth and micelle reshaping.¹⁸ In the current research, however, a simple and powerful model independent parameter, the invariant, is proposed here to quantitatively visualize the growth kinetics of MSNs.

The classical theory of Porod invariant indicates the phase evolution of a two-phase system.³⁹ In this paper, the synthesis of MSNs contains three phases, namely silica, solvent and micelles (SI Figure S2). For this three-phase system, the Porod invariant can be written as⁴¹

$$\text{Invariant} = 2\pi^2(\varphi_1\varphi_2\Delta\rho_{1,2}^2 + \varphi_1\varphi_3\Delta\rho_{1,3}^2 + \varphi_2\varphi_3\Delta\rho_{2,3}^2) \quad (6)$$

where, φ_1 , φ_2 , and φ_3 are the volume fraction of silica, solvent and micelles, respectively; $\Delta\rho_{1,2}$ is the SLD difference between silica and solvent, $\Delta\rho_{1,3}$ the SLD difference between silica and micelles and $\Delta\rho_{2,3}$ the SLD difference between micelles and solvent. The SLD of solvent and CTAB micelles are 9.44×10^{-6} and 9.21×10^{-6} Å⁻², respectively. It is therefore assumed that $\Delta\rho_{2,3}$ tends to be 0 and $\Delta\rho_{1,2}$ is approximately equal to $\Delta\rho_{1,3}$. **Equation 6** can be simplified as follows.

$$\text{invariant} = 2\pi^2\varphi_1(\varphi_2 + \varphi_3)\Delta\rho_{1,2}^2 \quad (7)$$

Moreover, there are only three phases in this synthesis system and the sum of φ_2 and φ_3 is equal to the volume fraction of rest phase except for silica; thus, **eq 7** can be rewritten as

$$\text{invariant} = 2\pi^2\varphi_1(1 - \varphi_1)\Delta\rho_{1,2}^2 \quad (8)$$

This final approximation allows us to use Porod invariant to determine MSN growth.^{42,43}

The changes in the scattering invariant over reaction time are shown in **Figure 3A**. The structural development of MSNs is

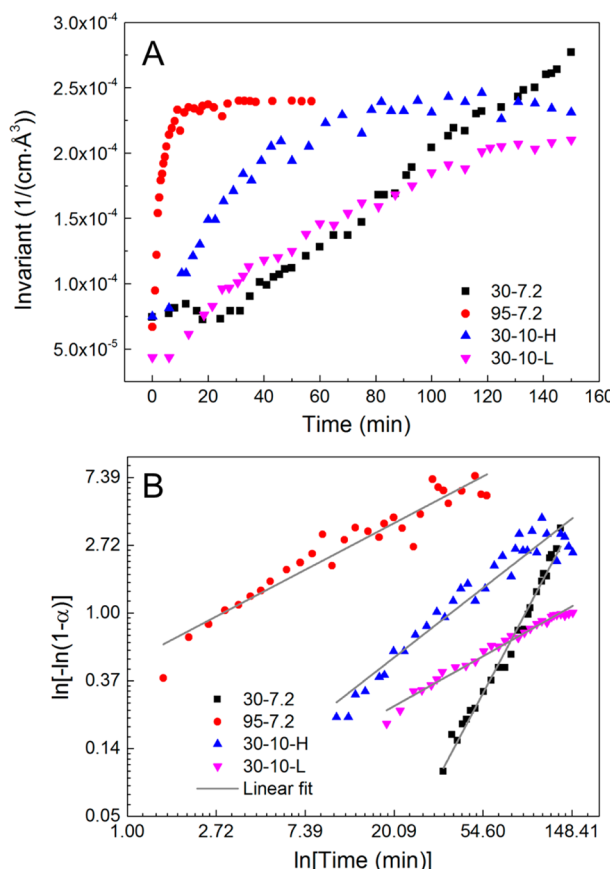


Figure 3. (A) MSN growth kinetics under different experimental conditions from the calculated invariant at characteristic time points. (B) Avrami plot and the corresponding linear fit for each sample. Both axes are formatted with the natural logarithm to fit in the Avrami equation.

associated with the generation of silica monomers by TEOS hydrolysis and their condensation onto CTAB micelles, which is related to a phase transformation from liquid (TEOS) to solid (silica). The Porod invariant is a measure of volume fraction of silica phase, which can link to the basic explanation of the Avrami equation. Hence, in this study, the Avrami

equation can be used to examine the kinetic parameters of MSN growth.^{20,44} The relation between the reaction rate and time is expressed in the following equation,

$$\alpha = 1 - e^{-kt^n} \quad (9)$$

where α is the fraction of invariant ((invariant at time t)/(invariant at the end)), t is the reaction time, k is the reaction constant, and n is a constant related to the growth mechanism and dimensions. Taking a mathematic transformation in eq 9, it is given

$$\ln[-\ln(1 - \alpha)] = \ln k + n \ln t \quad (10)$$

The reaction related constants (k and n) can be calculated from the intercept and slope of the linear fit in a $\ln[-\ln(1 - \alpha)]$ vs $\ln t$ plot that is shown in Figure 3B. The regression coefficients are all over 0.9 for the linear fitting. The calculated results from the linear fittings have been listed in Table 2.

Table 2. Reaction Constants Calculated from the Linear Fitting of Avrami Plot^a

samples	n	k	R^2
30-7.2	2.47	1.53×10^{-5}	0.98
95-7.2	0.73	0.69	0.92
30-10-H	1.02	0.023	0.92
30-10-L	0.73	0.028	0.98

^aNote: The values of n and k are obtained from the slope and intercept respectively in the linear fitting of Avrami plot.

The growth rate of MSNs is dependent on the experimental conditions such as temperature and pH. First, high temperature dramatically accelerates the growth rate of MSNs. The reaction constant k of sample 30–7.2 is the lowest among the series at 1.53×10^{-5} , while the high temperature (95 °C) provides the fastest reaction rate ($k = 0.69$) among all the four samples. This is because as the temperature increases, the molecules move faster and their contact frequency increases, leading to a faster reaction rate. Second, the reaction constants in samples 30-10-H and 30-10-L were found to exhibit similar magnitudes. This is likely related to similar hydrolysis and condensation rates for TEOS under the same pH (10) and temperature (30 °C). Third, the increase in reaction constant from 1.53×10^{-5} (30–7.2) to 0.023 (30–10-H) indicates a high formation rate of silica at pH 10. With the increase of pH value from 7.2 to 10 in the buffer solution, the hydrolysis rate of TEOS increases while the condensation rate decreases.⁴⁵ But the condensation rate is always faster than hydrolysis rate under basic condition, which makes the hydrolysis rate a determinant for the final rate of silica growth. Thus, a high silica growth rate was observed when increasing the pH value. In summary, the MSN growth rate was dependent on the reaction temperature and the pH of the system solution. A higher temperature and a higher pH value lead to a faster growth rate which is in good agreement with previous studies on the growth of silica nanoparticles.^{12,18} The use of the invariant offers a more efficient and simpler method to compare complex nanoparticle growth models by providing an estimation of the volume fraction of silica formed.

3.2. Growth Mechanism of MSNs. *3.2.1. Interaction between TEOS and Micelles.* SAXS data were collected before and after TEOS addition once the solution had stabilized at 80 °C for 30 min, to investigate the structural changes of CTAB micelles. After the addition of TEOS, the first SAXS pattern in the monitoring of MSN growth was examined, to study the

structure when the hydrolysis and condensation of TEOS had not greatly affected the scattering (Figure 4). The MSN growth of sample 95–7.2 was shown to complete within 2.5 min (Figure 2). This fast reaction rate made it difficult to capture the initial growth stage after TEOS addition. The data from this sample was therefore not modeled.

Before the addition of TEOS, the CTAB micellar structure is dependent on the ionic strength of the reaction solution (the left column of Figure 4A). The phosphate buffer solutions exhibited a similar ionic strength to samples 30-7.2 and 30-10-H; hence, the SAXS patterns of these samples displayed similar peak positions at 0.12 \AA^{-1} . In ammonia solution at a very low ionic strength, a different scattering pattern was found, which suggests that the shape of CTAB micelles in the no added salt conditions was different from that in the salt solution. The shape of micelles is affected by the screening charge that is not only from bromide counterions, but also from the added salt which causes the changes in the structure factor. The size, ellipticity, and shell thickness of CTAB micelles were obtained from the modeling (Table 3). It can be seen that even though the scattering patterns are different between the samples with and without salt, at 30 °C, the major radii of the core and the ellipticity remain the same at 25 Å and 0.55, respectively. Similar to the shape of the scattering patterns, the shell thickness of the micelles is around 12 Å in the phosphate buffer solution, while it is 10 Å in ammonia solution, which is the evidence of the absorption of counter-ions from the added salt.

Before starting the modeling of the SAXS data after TEOS addition, several simple assumptions were made in order to better interpret the effects of TEOS on the structure of CTAB micelles. First, the peaks for all the samples shifted to low Q with the increase in intensity (the right column in Figure 4A), and a small peak was also present at 0.22 \AA^{-1} after TEOS addition. This phenomenon is associated with the change of the micellar shape from ellipse to sphere according to the model for these two shapes calculated by the software (SI Figure S3). Second, it is assumed that TEOS solubilized in the hydrophobic core of CTAB micelles slightly expands the micelles, as it is reported that TEOS molecules were possible to solubilize in the hydrophobic core of surfactant at the initial stage.^{40,46} These studies provided the evidence to support this assumption. Third, to determine the proportion of TEOS solubilized in the cores, the results from growth kinetics (Figures 2 and 3) were taken into account. The MSN growth reached plateaus after 75 min for the sample synthesized at 30 °C (Figures 2 and 3). Thus the initial hydrolysis rate of TEOS (within 1 min) was very low. We assumed that 5% of TEOS was hydrolyzed in the aqueous solution after the consideration of reported reaction rate of TEOS⁴⁷ and the experimental setup in this work. This percentage is an upper bound and could be even less. In other words, more than 95% of TEOS was solubilized in the CTAB cores.

The SAXS data was fitted based on the above assumptions. A $P(Q)$ of sphere core–shell model was convolved with an $S(Q)$ of Hayter–Penfold RMSA to provide a fit to the data. It was assumed that the TEOS was solubilized in the hydrophobic cores of CTAB, and the SLD and the volume fraction of the CTAB core were recalculated as per the amount of TEOS solubilized. The input parameters and the best fit are shown in SI Table S1 and in Figure 4A, respectively. The sphere core–shell model worked well for all the samples with the addition of TEOS. The fitting of the SAXS data focused on Q range from 0.03 to 0.45 \AA^{-1} . The fitted parameters from the model are

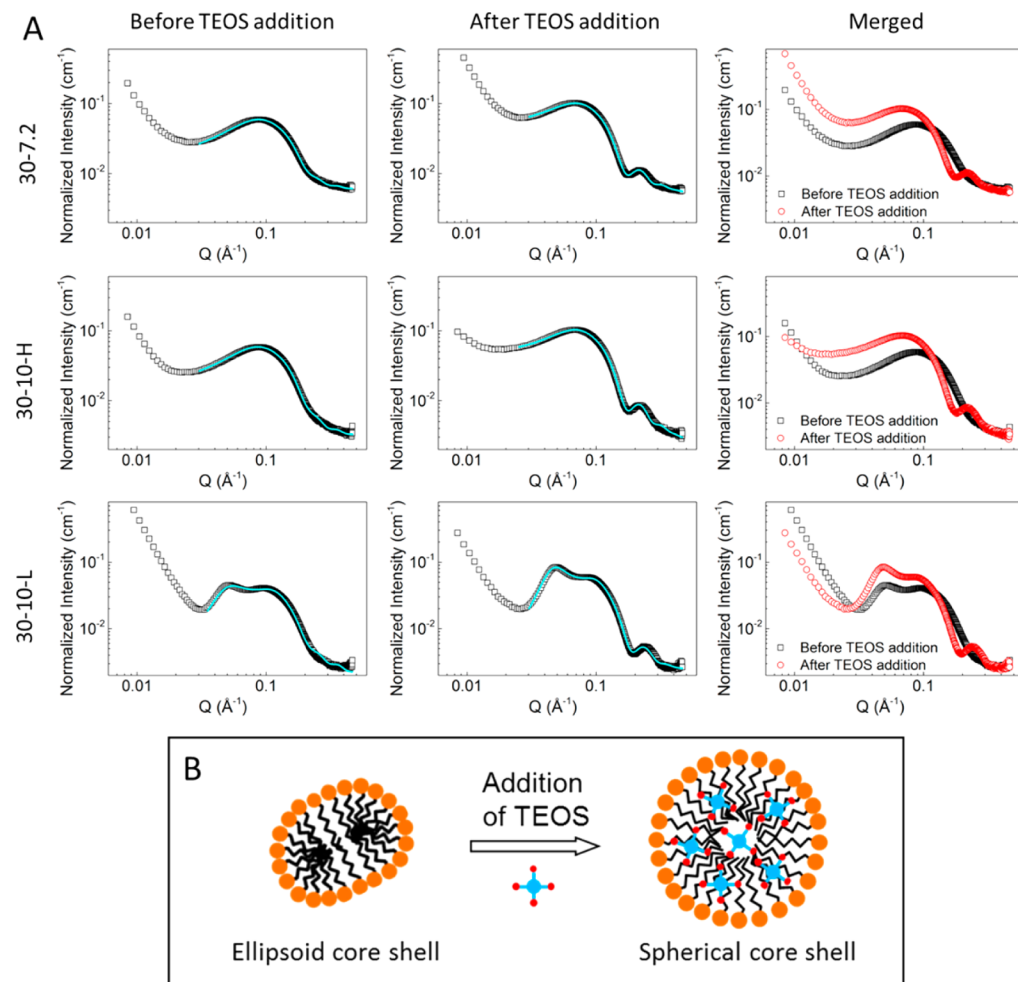


Figure 4. SAXS data and model fitting before and after TEOS addition (A). Raw SAXS data is shown in empty square (before) and circle (after). Continuous lines represent the fitting according to the model. Merged graphs are shown in the right column. Schematic view of the structural change of CTAB micelles before and after TEOS addition (B).

Table 3. Summary of CTAB Structural Parameters Calculated for Fitting SAXS Data before and after TEOS Addition

samples	major radius of core (Å)	axial ratio ^a	shell thickness (Å)
before TEOS addition			
30-7.2	25.3	0.55	12.4
30-10-H	25.4	0.55	12.6
30-10-L	25.6	0.57	10.0
after TEOS addition ^b (95% TEOS solubilization)			
30-7.2	28.6	1	5.7
30-10-H	29.1	1	4.3
30-10-L	24.1	1	11.2

^aThe axial ratio is the major to minor axis ratio. It is 1 for spheres. ^bA radius polydispersity of 0.1 was introduced to obtain the best fit after TEOS addition.

shown in Table 3. It can be seen from the results that the radii are all above the critical chain length of hydrocarbon core (21.8 Å⁴⁸), which might be attributed to the solubilization of TEOS in the hydrocarbon cores (Figure 4B). Furthermore, the size of mesopores at the final stage of MSN growth decreases probably due to the shrinking of the micelles as TEOS consumed during hydrolysis and condensation. The diffraction peak at around 0.15 Å⁻¹ (Figure 2C, F, I, and L) indicated the mesopore size,

which corresponds to a real space dimension of 4.1 nm. The size of mesopores was smaller than the initial micellar diameter of 5.5 nm for 30-7.2, 4.6 nm for 95-7.2, 5.5 nm for 30-10-H, and 4.7 nm for 30-10-L, after TEOS addition, which shows the shrinking of micelles during the growth of MSNs.

3.2.2. Proposed Growth Mechanism: Swelling–Shrinking Model. The existing studies on the mechanism of MSN growth illustrate that silica monomers absorb onto micelles and then the condensation of silica monomer induces the aggregation of micelles to form particles.^{12,13,15} The location of TEOS is missing in previous studies. The synthesis of MSNs is always conducted in aqueous solution and the TEOS is an oil-like monomer. According to our experiments, the phase separation was observed in CTAB solution under static conditions (without stirring), while under vigorous stirring, a turbid emulsion-like system was formed without phase separation. The role of TEOS has not been well investigated, and based on the existing theory of MSN growth and the above results, we proposed a potentially new mechanism of MSN growth, which is shown in Figure 5.

Based on the understanding of the effects of TEOS on micellar structure and the existing mechanism studies,^{18,27,49,50} we proposed a possible model, the “swelling–shrinking” model to explain the growth mechanism. The detailed description is as follows. (1) Before the addition of TEOS, ellipsoidal CTAB

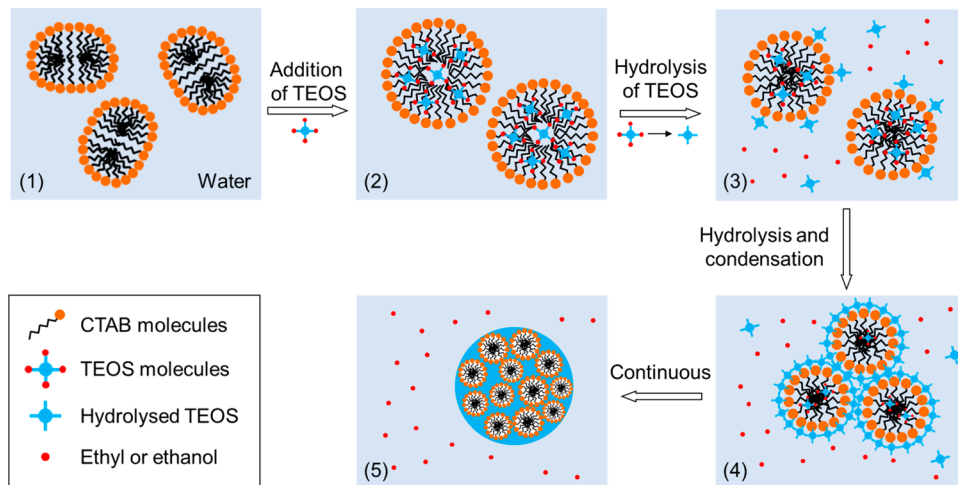


Figure 5. Schematic of the structural changes of CTAB micelles before and after TEOS addition. Red dots represent ethyl groups in TEOS molecules and ethanol in aqueous solution after the hydrolysis of TEOS.

micelles self-assemble⁵¹ (step (1) in Figure 5). The micelles are positively charged due to the head groups of the quaternary ammonium salt in the CTAB molecules. The core of CTAB micelles is formed by hydrocarbon tails that are hydrophobic. (2) After the addition of TEOS, oil-like TEOS is solubilized in the hydrophobic core of CTAB micelles, leading to the enlarged size and micellar shape changes (from ellipsoid to spherical) (step (2) in Figure 5) based on the assumption made in the above section. The presence of TEOS in micelle cores is also likely to lead to a polydispersity in micelle size.⁵² (3) The silica monomers become hydrophilic with the hydrolysis of TEOS and are progressively released into the aqueous solution (step (3) in Figure 5). There are two possible pathways for TEOS in the hydrophobic cores contacting with water molecules. The existing reports have suggested that there are only a limited water molecules that penetrate into the hydrocarbon core,^{53,54} which is one of the possible pathways for the hydrolysis of TEOS. On the other hand, the extensive water contacts with hydrocarbon core at the interface between hydrocarbon core and water,⁵⁵ is another more likely pathway for the hydrolysis of TEOS. Within the oil-like CTAB core, the TEOS molecules can move freely and have a chance to contact with water at the interface to be hydrolyzed. This pathway is similar to the hydrolysis of TEOS from the droplet of TEOS phase in the aqueous solution, in which case the molecules at the interface have the priority to be hydrolyzed.⁵⁵ The model of TEOS in hydrocarbon core can be treated as a diluted TEOS liquid by CTAB tails. Since the hydrolyzed silica monomers are negatively charged, they are adsorbed onto positively charged CTAB micelles electrostatically. With the consumption of TEOS in CTAB core, the micelles shrink and the size becomes smaller. As another product of hydrolysis, ethanol is also present in the solution. The amount of produced ethanol is 0.032 mol from 0.008 mol of TEOS. (4) The hydrolysis and condensation of silica happens simultaneously.⁵⁶ Silica monomers gradually release from the core of micelles and form a silica shell around micelles (step (4) in Figure 5). During this process, the micelles continue to shrink until all the TEOS in the core is hydrolyzed. The neighboring micelles with a silica shell start to aggregate, which produces the nuclei for the particle growth. (5) Finally, with the growth of nuclei and continuous hydrolysis and condensation, silica forms a strong framework, and particles and mesopores form. In summary, the

growth of MSN starts from swollen micelles, followed by continuous shrinking of micelles. This mechanism can be used to explain the synthesis with only TEOS as precursor but without any other solvent, such as ethanol, to assist TEOS to dissolve in aqueous solution.

4. CONCLUSIONS

Time-resolved SAXS with a synchrotron source was employed to study the growth mechanism of MSNs. The influence of solution temperature, pH and ionic strength on growth kinetics of the MSNs was systematically investigated. The growth kinetics of MSNs was investigated through the scattering invariant which was proved to be an efficient and powerful tool to estimate the growth kinetics of MSNs. The results showed that higher temperatures and pH offer faster reaction rates, which was attributed to the acceleration of MSN growth. The modeling results suggested that the CTAB micelle size is expanded and the micellar shape changes, due to the solubilization of TEOS in CTAB hydrocarbon cores. To explain our observation a swelling–shrinking model was proposed for the first time to interpret the MSN growth based on the investigation of structural evolution under time-resolved SAXS, which may provide useful information for the location of TEOS during the synthesis. This model provides a new insight into an understanding of the MSN growth mechanism and has the potential to make a theoretical contribution to nanoparticle synthesis from surfactant templates.

ASSOCIATED CONTENT

S Supporting Information

Tables showing input parameters for modeling of CTAB micelles before and after TEOS addition, and scattering length density of chemicals used in this study and figures showing representative TEM images of MSNs, schematic of phases during MSN growth, and model calculated curve with different form factor. The Supporting Information is available free of charge on the ACS Publications website at DOI: 10.1021/acs.langmuir.5b01637.

AUTHOR INFORMATION

Corresponding Authors

*E-mail: cjg@ansto.gov.au.

*E-mail: lingxue.kong@deakin.edu.au.

Notes

The authors declare no competing financial interest.

ACKNOWLEDGMENTS

The authors would like to acknowledge the beamtime provided by the Australian Synchrotron under Grants M5826 in March 2013 and M6410 in August 2013. Zhifeng Yi has been supported by a Deakin University DUPRS scholarship. Dr. Dumée acknowledges Deakin University for funding his Alfred Deakin Postdoctoral Fellowship. We thank Rosey Van Driel at the Institute for Frontier Materials, Deakin University for her help with transmission electron microscopy.

REFERENCES

- (1) Meynen, V.; Cool, P.; Vansant, E. F. Verified Syntheses of Mesoporous Materials. *Microporous Mesoporous Mater.* **2009**, *125* (3), 170–223.
- (2) Tang, F.; Li, L.; Chen, D. Mesoporous Silica Nanoparticles: Synthesis, Biocompatibility and Drug Delivery. *Adv. Mater.* **2012**, *24* (12), 1504–1534.
- (3) Vivero-Escoto, J. L.; Slowing, I. I.; Trewyn, B. G.; Lin, V. S. Y. Mesoporous Silica Nanoparticles for Intracellular Controlled Drug Delivery. *Small* **2010**, *6* (18), 1952–1967.
- (4) Wu, S.-H.; Mou, C.-Y.; Lin, H.-P. Synthesis of Mesoporous Silica Nanoparticles. *Chem. Soc. Rev.* **2013**, *42* (9), 3862–3875.
- (5) Trewyn, B. G.; Slowing, I. I.; Giri, S.; Chen, H.-T.; Lin, V. S. Y. Synthesis and Functionalization of a Mesoporous Silica Nanoparticle Based on the Sol–Gel Process and Applications in Controlled Release. *Acc. Chem. Res.* **2007**, *40* (9), 846–853.
- (6) Sun, D.; Hussain, H. I.; Yi, Z.; Siegele, R.; Cresswell, T.; Kong, L.; Cahill, D. M. Uptake and Cellular Distribution, in Four Plant Species, of Fluorescently Labeled Mesoporous Silica Nanoparticles. *Plant Cell Rep.* **2014**, *33* (8), 1389–402.
- (7) Hussain, H.; Yi, Z.; Rookes, J.; Kong, L.; Cahill, D. Mesoporous Silica Nanoparticles as a Biomolecule Delivery Vehicle in Plants. *J. Nanopart. Res.* **2013**, *15* (6), 1676–1690.
- (8) Yi, Z.; Hussain, H. I.; Feng, C.; Sun, D.; She, F.; Rookes, J. E.; Cahill, D. M.; Kong, L. Functionalized Mesoporous Silica Nanoparticles with Redox-Responsive Short-Chain Gatekeepers for Agrochemical Delivery. *ACS Appl. Mater. Interfaces* **2015**, *7* (18), 9937–46.
- (9) Urata, C.; Aoyama, Y.; Tonegawa, A.; Yamauchi, Y.; Kuroda, K. Dialysis Process for the Removal of Surfactants to Form Colloidal Mesoporous Silica Nanoparticles. *Chem. Commun.* **2009**, *34*, 5094–5096.
- (10) Chiang, Y.-D.; Lian, H.-Y.; Leo, S.-Y.; Wang, S.-G.; Yamauchi, Y.; Wu, K. C. W. Controlling Particle Size and Structural Properties of Mesoporous Silica Nanoparticles Using the Taguchi Method. *J. Phys. Chem. C* **2011**, *115* (27), 13158–13165.
- (11) Ma, K.; Sai, H.; Wiesner, U. Ultrasmall Sub-10 Nm near-Infrared Fluorescent Mesoporous Silica Nanoparticles. *J. Am. Chem. Soc.* **2012**, *134* (32), 13180–13183.
- (12) Blin, J. L.; Imperor-Clerc, M. Mechanism of Self-Assembly in the Synthesis of Silica Mesoporous Materials: In Situ Studies by X-Ray and Neutron Scattering. *Chem. Soc. Rev.* **2013**, *42* (9), 4071–4082.
- (13) Gao, C.; Qiu, H.; Zeng, W.; Sakamoto, Y.; Terasaki, O.; Sakamoto, K.; Chen, Q.; Che, S. Formation Mechanism of Anionic Surfactant-Templated Mesoporous Silica. *Chem. Mater.* **2006**, *18* (16), 3904–3914.
- (14) Flodström, K.; Wennerström, H.; Alfredsson, V. Mechanism of Mesoporous Silica Formation. A Time-Resolved Nmr and Tem Study of Silica–Block Copolymer Aggregation. *Langmuir* **2004**, *20* (3), 680–688.
- (15) Suteewong, T.; Sai, H.; Hovden, R.; Muller, D.; Bradbury, M. S.; Gruner, S. M.; Wiesner, U. Multicompartment Mesoporous Silica Nanoparticles with Branched Shapes: An Epitaxial Growth Mechanism. *Science* **2013**, *340* (6130), 337–341.
- (16) Wang, R.-H.; Sun, J. The Growth Mechanism of Continuous Cubic Mesoporous Sba-16 Film with a Large Area of Highly Ordered Pores. *Nanotechnology* **2007**, *18* (18), 185705.
- (17) Gianotti, E.; Berlier, G.; Costabello, K.; Coluccia, S.; Meneau, F. In Situ Synchrotron Small-Angle X-Ray Scattering Study of Mcm-41 Crystallisation Using Gemini Surfactants. *Catal. Today* **2007**, *126* (1–2), 203–210.
- (18) Hollamby, M. J.; Borisova, D.; Brown, P.; Eastoe, J.; Grillo, I.; Shchukin, D. Growth of Mesoporous Silica Nanoparticles Monitored by Time-Resolved Small-Angle Neutron Scattering. *Langmuir* **2012**, *28* (9), 4425–4433.
- (19) Tolbert, S. H. Mesoporous Silica: Holey Quasicrystals. *Nat. Mater.* **2012**, *11* (9), 749–751.
- (20) Tobler, D. J.; Shaw, S.; Benning, L. G. Quantification of Initial Steps of Nucleation and Growth of Silica Nanoparticles: An in-Situ Sacs and Dls Study. *Geochim. Cosmochim. Acta* **2009**, *73* (18), 5377–5393.
- (21) Kirby, N. M.; Mudie, S. T.; Hawley, A. M.; Cookson, D. J.; Mertens, H. D. T.; Cowieson, N.; Samardzic-Boban, V. A Low-Background-Intensity Focusing Small-Angle X-Ray Scattering Undulator Beamline. *J. Appl. Crystallogr.* **2013**, *46* (6), 1670–1680.
- (22) Chen, Z. H.; Kim, C.; Zeng, X.-b.; Hwang, S. H.; Jang, J.; Ungar, G. Characterizing Size and Porosity of Hollow Nanoparticles: Sacs, Sans, Tem, Dls, and Adsorption Isotherms Compared. *Langmuir* **2012**, *28* (43), 15350–15361.
- (23) Schmitt, J.; Impérator-Clerc, M.; Michaux, F.; Blin, J.-L.; Stébé, M.-J.; Pedersen, J. S.; Meneau, F. Formation of Nanostructured Silica Materials Templated with Nonionic Fluorinated Surfactant Followed by in Situ Sacs. *Langmuir* **2013**, *29* (6), 2007–2023.
- (24) Manet, S.; Schmitt, J.; Impérator-Clerc, M.; Zholobenko, V.; Durand, D.; Oliveira, C. L. P.; Pedersen, J. S.; Gervais, C.; Baccile, N.; Babonneau, F.; Grillo, I.; Meneau, F.; Rochas, C. Kinetics of the Formation of 2d-Hexagonal Silica Nanostructured Materials by Nonionic Block Copolymer Templating in Solution. *J. Phys. Chem. B* **2011**, *115* (39), 11330–11344.
- (25) Sundblom, A.; Oliveira, C. L. P.; Palmqvist, A. E. C.; Pedersen, J. S. Modeling in Situ Small-Angle X-Ray Scattering Measurements Following the Formation of Mesostructured Silica. *J. Phys. Chem. C* **2009**, *113* (18), 7706–7713.
- (26) Alsyouri, H.; Abu-Daabes, M.; Alassali, A.; Lin, J. Ordered Mesoporous Silica Prepared by Quiescent Interfacial Growth Method - Effects of Reaction Chemistry. *Nanoscale Res. Lett.* **2013**, *8* (1), 484.
- (27) Michaux, F.; Baccile, N.; Impérator-Clerc, M.; Malfatti, L.; Folliet, N.; Gervais, C.; Manet, S.; Meneau, F.; Pedersen, J. S.; Babonneau, F. In Situ Time-Resolved Sacs Study of the Formation of Mesostructured Organically Modified Silica through Modeling of Micelles Evolution During Surfactant-Templated Self-Assembly. *Langmuir* **2012**, *28* (50), 17477–17493.
- (28) Liu, C.; Wang, X.; Lee, S.; Pfefferle, L. D.; Haller, G. L. Surfactant Chain Length Effect on the Hexagonal-to-Cubic Phase Transition in Mesoporous Silica Synthesis. *Microporous Mesoporous Mater.* **2012**, *147* (1), 242–251.
- (29) Nooney, R. I.; Thirunavukkarasu, D.; Chen, Y.; Josephs, R.; Ostafin, A. E. Synthesis of Nanoscale Mesoporous Silica Spheres with Controlled Particle Size. *Chem. Mater.* **2002**, *14* (11), 4721–4728.
- (30) He, Q.; Cui, X.; Cui, F.; Guo, L.; Shi, J. Size-Controlled Synthesis of Monodispersed Mesoporous Silica Nano-Spheres under a Neutral Condition. *Microporous Mesoporous Mater.* **2009**, *117* (3), 609–616.
- (31) Zana, R.; Lévy, H.; Danino, D.; Talmon, Y.; Kwetkat, K. Mixed Micellization of Cetyltrimethylammonium Bromide and an Anionic Dimeric (Gemini) Surfactant in Aqueous Solution. *Langmuir* **1997**, *13* (3), 402–408.

- (32) Ma, K.; Werner-Zwanziger, U.; Zwanziger, J.; Wiesner, U. Controlling Growth of Ultrasmall Sub-10 Nm Fluorescent Mesoporous Silica Nanoparticles. *Chem. Mater.* **2013**, *25* (5), 677–691.
- (33) Pedersen, J. S. Analysis of Small-Angle Scattering Data from Micelles and Microemulsions: Free-Form Approaches and Model Fitting. *Curr. Opin. Colloid Interface Sci.* **1999**, *4* (3), 190–196.
- (34) Berr, S. S. Solvent Isotope Effects on Alkytrimethylammonium Bromide Micelles as a Function of Alkyl Chain Length. *J. Phys. Chem.* **1987**, *91* (18), 4760–4765.
- (35) Kotlarchyk, M.; Chen, S. H. Analysis of Small Angle Neutron Scattering Spectra from Polydisperse Interacting Colloids. *J. Chem. Phys.* **1983**, *79* (5), 2461–2469.
- (36) Hansen, J.-P.; Hayter, J. B. A Rescaled Msa Structure Factor for Dilute Charged Colloidal Dispersions. *Mol. Phys.* **1982**, *46* (3), 651–656.
- (37) Hayter, J. B.; Penfold, J. An Analytic Structure Factor for Macroion Solutions. *Mol. Phys.* **1981**, *42* (1), 109–118.
- (38) Griffiths, P. C.; Paul, A.; Heenan, R. K.; Penfold, J.; Ranganathan, R.; Bales, B. L. Role of Counterion Concentration in Determining Micelle Aggregation: Evaluation of the Combination of Constraints from Small-Angle Neutron Scattering, Electron Paramagnetic Resonance, and Time-Resolved Fluorescence Quenching. *J. Phys. Chem. B* **2004**, *108* (12), 3810–3816.
- (39) Guinier, A.; Fournet, G. *Small-Angle Scattering of X-Rays*; John Wiley & Sons Inc: New York, 1955.
- (40) Ågren, P.; Lindén, M.; Rosenholm, J. B.; Schwarzenbacher, R.; Kriechbaum, M.; Amenitsch, H.; Laggner, P.; Blanchard, J.; Schüth, F. Kinetics of Cosurfactant–Surfactant–Silicate Phase Behavior. 1. Short-Chain Alcohols. *J. Phys. Chem. B* **1999**, *103* (29), 5943–5948.
- (41) Ciccarello, S.; Melnichenko, Y. B.; He, L. Supercritical Carbon Dioxide Behavior in Porous Silica Aerogel. *J. Appl. Crystallogr.* **2011**, *44* (1), 43–51.
- (42) McDermott, A. G.; Budd, P. M.; McKeown, N. B.; Colina, C. M.; Runt, J. Physical Aging of Polymers of Intrinsic Microporosity: A Saks/Waxs Study. *J. Mater. Chem. A* **2014**, *2* (30), 11742–11752.
- (43) Kwon, S. G.; Krylova, G.; Phillips, P. J.; Klie, R. F.; Chattopadhyay, S.; Shibata, T.; Bunel, E. E.; Liu, Y.; Prakapenka, V. B.; Lee, B.; Shevchenko, E. V. Heterogeneous Nucleation and Shape Transformation of Multicomponent Metallic Nanostructures. *Nat. Mater.* **2015**, *14* (2), 215–223.
- (44) Chae, K.; Shi, Y.; Huang, L. Nanocasting of Hierarchical Nanostructured Porous Carbon in Molecular Dynamics Simulation. *J. Mater. Chem. A* **2013**, *1* (12), 3886–3894.
- (45) Boissière, C.; Larbot, A.; van der Lee, A.; Kooyman, P. J.; Prouzet, E. A New Synthesis of Mesoporous Msu-X Silica Controlled by a Two-Step Pathway. *Chem. Mater.* **2000**, *12* (10), 2902–2913.
- (46) Edler, K. J. Mesoporous Silicates. In *Porous Materials*; Bruce, D. W., O'Hare, D., Walton, R. I., Eds.; John Wiley & Sons, Ltd: New York, 2010; pp 69–145.
- (47) Chang, C.-L.; Fogler, H. S. Kinetics of Silica Particle Formation in Nonionic W/O Microemulsions from Teos. *AIChE J.* **1996**, *42* (11), 3153–3163.
- (48) Tanford, C. Theory of Micelle Formation in Aqueous Solutions. *J. Phys. Chem.* **1974**, *78* (24), 2469–2479.
- (49) Zholobenko, V. L.; Khodakov, A. Y.; Impérator-Clerc, M.; Durand, D.; Grillo, I. Initial Stages of Sba-15 Synthesis: An Overview. *Adv. Colloid Interface Sci.* **2008**, *142* (1–2), 67–74.
- (50) Sundblom, A.; Oliveira, C. L. P.; Pedersen, J. S.; Palmqvist, A. E. C. On the Formation Mechanism of Pluronic-Templated Mesostructured Silica. *J. Phys. Chem. C* **2010**, *114* (8), 3483–3492.
- (51) Warr, G. G.; Zemb, T. N.; Drifford, M. Liquid-Liquid Phase Separation in Cationic Micellar Solutions. *J. Phys. Chem.* **1990**, *94* (7), 3086–3092.
- (52) Israelachvili, J. N.; Mitchell, D. J.; Ninham, B. W. Theory of Self-Assembly of Hydrocarbon Amphiphiles into Micelles and Bilayers. *J. Chem. Soc., Faraday Trans. 2* **1976**, *72* (0), 1525–1568.
- (53) Bendedouch, D.; Chen, S. H.; Koehler, W. C. Structure of Ionic Micelles from Small Angle Neutron Scattering. *J. Phys. Chem.* **1983**, *87* (1), 153–159.
- (54) Chen, S. H.; Dill, K. Water in the Hydrocarbon Core of Micelles (Reply). *Nature* **1985**, *314* (6009), 385–386.
- (55) Moroi, Y. *Micelles: Theoretical and Applied Aspects*; Springer: New York, 2013.
- (56) Brinker, C. J. Hydrolysis and Condensation of Silicates: Effects on Structure. *J. Non-Cryst. Solids* **1988**, *100* (1–3), 31–50.